

Synthesis and gas sensor applications of nanostructured ZnO grown at low temperatures

Oleg LUPAN^{1,2,3,*}, Thierry PAUPORTÉ², Lee CHOW³

¹Department of Microelectronics and Biomedical Engineering, Technical University of Moldova, Chisinau, Moldova

²Institut de Recherche de Chimie-Paris, CNRS-Chimie Paris UMR8247, 11 rue Pierre et Marie Curie, 75005 Paris, France

³Department of Physics, University of Central Florida, Orlando, FL, USA

Received: 29.06.2014 • Accepted: 24.09.2014 • Published Online: 10.11.2014 • Printed: 28.11.2014

Abstract: ZnO nanoarchitecture-based nano- and microdevices came into the focus due to their multifunctional operation. In this work, we summarize cost-effective procedures to grow ZnO nano- and microstructures, namely hydrothermal growth and electrochemical deposition. These techniques allow the controllable growth of ZnO nano- and microarchitectures at relatively low temperatures, below 100 °C, and do not require sophisticated equipment. We report on technological details for synthesis of ZnO and its characterization and applications in different novel devices such as gas sensors. Nanosensors and microsensors were fabricated using a focused ion beam and by metal welding an individual nano- and microstructure to form rigid contacts. Devices made from pure and doped ZnO nanostructures are presented and discussed. Developed nano- and microdevice structures show promising performances and are quite attractive for further investigations in sensor applications. Several factors determine the gas sensing mechanism of pure and doped ZnO micro- and nanowire/nanorods and discussions on this are summarized.

Key words: ZnO, nanosensor, microdevices, electrochemical, hydrothermal

1. Introduction

At present, there exists emerging interest in the synthesis and applications of ZnO nanomaterials at relatively lower temperatures, especially below 100 °C. ZnO is a key multifunctional material exhibiting semiconducting, magnetic, and piezoelectric properties [1,2]. It has a wide direct band gap of 3.37 eV at 300 K, large exciton binding energy of 60 meV, and excellent chemical, mechanical, and thermal stability and biocompatibility [1–4]. New devices based on nanoarchitectures such as nanowires, nanotubes, and nanorods have attracted vast and persistent attention for a variety of applications, including detecting ultraviolet (UV) radiation, gas sensing, and detecting chemical and biological molecules [1–8]. It is of major interest to fabricate new multifunctional devices. That is why it is important to develop a well-controlled technology to grow ZnO that exhibits the most abundant configurations of nanostructures. In this work, we will review some cost-effective procedures to grow ZnO nano- and microstructures at relatively lower temperatures below 100 °C and their characterization, sensing mechanisms, and applications in different device structures.

*Correspondence: oleg.lupan@chimie-paristech.fr

2. Hydrothermal growth of ZnO nano- and microstructures

2.1. Experimental details on growth of pure ZnO nano- and microstructures

The previous work by Lupan et al. [4] reported a technology that permits rapid and controlled growth of ZnO nano- and microrod arrays of 1D rods, 2D crosses, and 3D tetrapods without the use of templates or seeds. In this case, zinc sulfate $[\text{Zn}(\text{SO}_4) \cdot 7\text{H}_2\text{O}]$ and ammonia (NH_4OH) (Fisher Scientific, reagent grade, without further purification) were used for the synthesis of ZnO nano- and microarchitectures, and 0.1–0.15 M $\text{Zn}(\text{SO}_4) \cdot 7\text{H}_2\text{O}$ and NH_4OH (29.6%) were mixed with 100 mL of deionized (DI) water until complete dissolution at room temperature, i.e. until the solution became colorless. The substrates were kept in a SnCl_2/HCl solution for 3–5 min and then rinsed with a jet of DI water. Finally, the glass, quartz, and Si substrates were placed inside an aqueous solution in a reactor, which consisted of a glass beaker (5 cm in diameter) with a spherical concave cap with a radius of curvature of 10 cm and an orifice (1 mm in radius) on the side. The setup was mounted on a hot plate, and the temperature was quickly increased to 90–95 °C and kept constant for 15 min without any stirring. Manipulation and reactions were carried out in air inside a fume hood. In this experiment, ZnO nano- and microcrystals were formed at a pH value of 10–11 [4].

The surface morphology of the rods was investigated by scanning electron microscopy (SEM). Typical

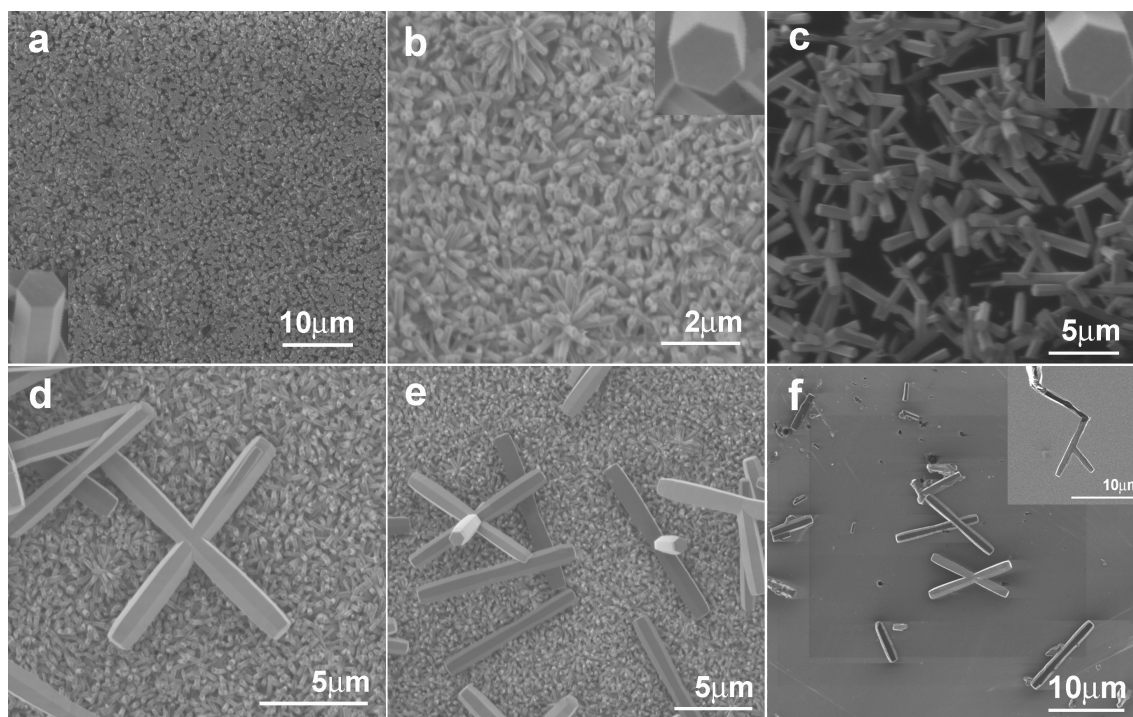


Figure 1. SEM images of the ZnO rods chemically grown from ZnSO_4 and ammonia aqueous bath on (a) glass substrates, (b) quartz substrates, and (c) Si substrates. The insets in Figures 1a–1c display single ZnO rods with hexagonal basis, while (d) corresponds to 2-dimensional 2D ZnO crosses; (e) to branched 1D, 2D, and 3D microrods with ZnO nanorod arrays as background; and (f) to 1D and 2D branched microrods transferred to another Si substrate, The inset in (f) shows an individual tripod picked up by the in situ lift-out needle in the focused ion beam (FIB) system. [Reprinted from *Materials Science and Engineering: B*, 145, O. Lupan, L. Chow, G. Chai, B. Roldan Cuenya, A. Naitabdi, A. Schulte, H. Heinrich, *Nanofabrication and characterization of ZnO nanorod arrays and branched microrods by aqueous solution route and rapid thermal processing*, 57-66, Copyright (2007), with permission from Elsevier]

SEM images of the ZnO nanorod arrays and individual microrods are shown in Figure 1 [4]. The overall morphology of the ZnO nanorod arrays on a glass substrate is shown in Figure 1a, which indicates that the obtained product consisted of nanorods with an average diameter of 300 nm. The lengths of the ZnO nanorods were about 2 μm . ZnO nanorods with diameters of 100 nm were also synthesized on quartz with the same method (Figure 1b). The morphology of the ZnO nanorods grown on Si is shown in Figure 1c. The SEM images of ZnO samples after rapid thermal processing at 650–750 $^{\circ}\text{C}$ do not differ from those shown in Figures 1a–1c. New 1D, 2D, and 3D ZnO branched microrods are presented in Figures 1d–1f. According to the experimental results, the branched architectures obtained by the proposed process can be easily transferred to other substrates and handled by focused ion beam (FIB) in order to fabricate different nano- and microdevices (Figure 1f). The inset in Figure 1f shows an individual tripod picked up by the in situ lift-out needle in the FIB system. The insets in Figures 1a–1c correspond to high-resolution SEM images taken of single rods and display the hexagonal base of nano- and microrods on different substrates [4].

The corresponding transmission electron microscopy (TEM) images and selective area electron diffraction (SAED) pattern of an individual ZnO nanorod are shown in Figures 2a and 2b. As indexed (Figure 2b) in the inset SAED pattern, the nanorod was grown along the direction of the (0 0 1) zone axis of ZnO, which agrees with the high-resolution TEM results [4]. The incident beam was along the zone axis. For other samples, similar high-resolution TEM results and SAED patterns were observed (Figure 2a). Please note that in Figure 2a, the sample is relatively thick and the spacing of 0.52 nm is referring to the unit cell along the c -axis, while in Figure 2b the spacing is showing half of the unit cell along the c -axis. This difference has to do with slight misalignment with the electron beam: in Figure 2a the electron beam is not exactly perpendicular to the c -axis, while in Figure 2b it is perpendicular to the c -axis. With TEM characterization we found that the nanorods and branched microrods were straight and with a smooth surface [4]. By employing a similar technique, different morphologies of ZnO nano- and microarchitectures were grown as reported in a previous work [5].

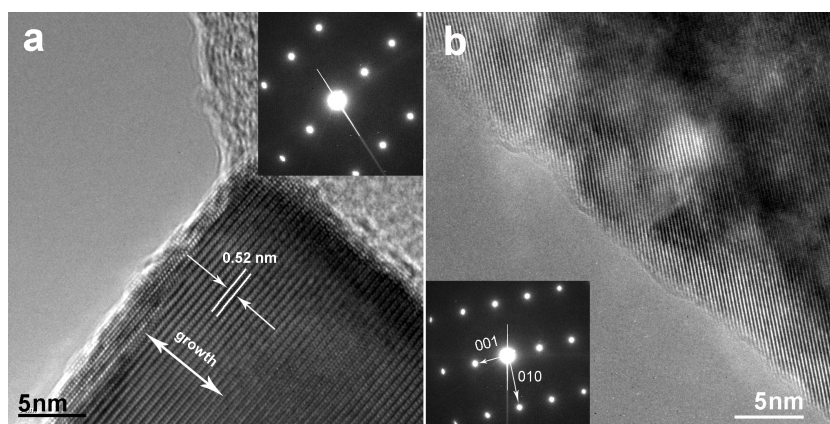


Figure 2. High-resolution TEM images when (a) the sample is relatively thick and (b) the spacing is showing half of the unit cell along the c -axis. The inset shows select area diffraction patterns of the crystalline ZnO nanorods grown by aqueous solution deposition. The diffraction patterns show that the nanorod grows along the (0001) direction. [Reprinted from *Materials Science and Engineering: B*, 145, O. Lupan, L. Chow, G. Chai, B. Roldan Cuenya, A. Naitabdi, A. Schulte, H. Heinrich, *Nanofabrication and characterization of ZnO nanorod arrays and branched microrods by aqueous solution route and rapid thermal processing*, 57-66, Copyright (2007), with permission from Elsevier]

2.2. Experimental details on hydrothermal growth of doped ZnO nano- and microstructures

For the synthesis of doped zinc oxide nanostructures it is important to have good control over the technological parameters to achieve the desired results. We will first summarize the experimental data reported by Chow et al. [6]. ZnO and Cu-doped ZnO low-dimensional rods were grown by a procedure discussed in detail in previous reports [4,9]. *P*-type Si (100) substrates were used for the synthesis of the ZnO and Cu-ZnO material. First the silicon (Si) substrates were cleaned as reported before [10,11]. Zinc sulfate heptahydrate was first dissolved in 100 mL of DI water, and then 50 mL of ammonia (29.3%, Fisher Scientific) was added and stirred for 10 min to mix completely at room temperature. The first set of pure ZnO nanorod (#1) samples was synthesized using 0.1–0.5 M $\text{Zn}(\text{SO}_4) \cdot 7\text{H}_2\text{O}$ [4]. The second set of samples (#2) was prepared using 0.1–0.5 M zinc sulfate and 0.001–0.005 M copper chloride (99.99%), which was dissolved in 100 mL of DI water. The $[\text{Cu}]/([\text{Zn}]+[\text{Cu}])$ ratio of copper dopants in the ZnO rods was controlled by changing the relative amount of Cu to Zn in the precursor solution. An ammonia solution (29.3%) was added until the solution became transparent and clear. Subsequently, the resulting aqueous solution was poured into a 120-mL reactor (75% filled) [4]. The vessel was placed on a preheated oven for 20 min at 95 °C and then allowed to cool down to room temperature in 40 min. After the reaction was completed, the grown ZnO nanorods on the substrates were rinsed in DI water for 2 min and then the samples were dried in air at 150 °C for 5 min. Manipulation and reactions were carried out in air inside a fume hood [4,6].

A systematic investigation of Cu-doping effects on the properties of ZnO quasi-one-dimensional structures was performed using several techniques [4,6]. The insert in Figure 3 shows the SEM image of Cu-doped ZnO grown by hydrothermal technique at 95 °C in 20 min. Low-dimensional rods of ZnO can be seen as agglomerations on the substrate. Later these structures can be transferred and dispersed on other substrates, as was described in previous works [4,6,8,9].

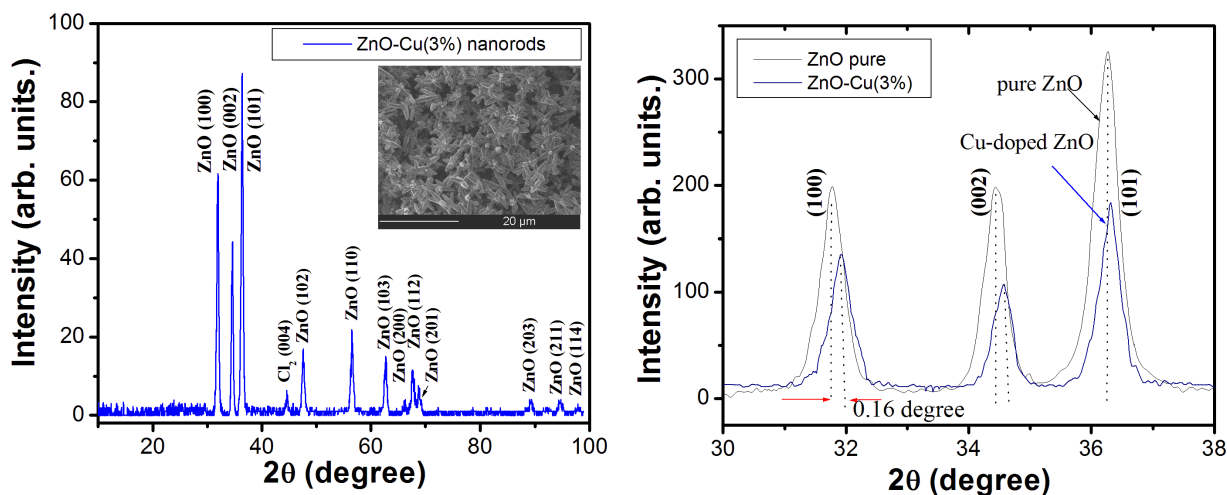


Figure 3. (a) XRD diffractogram of the 3% Cu-doped ZnO nanorods. Inset shows an SEM image of 3% Cu-doped ZnO low-dimensional rods on $\text{SiO}_2/\text{Si}(001)$. (b) Comparison of the (100), (002), and (101) XRD peaks for pure ZnO and 3% Cu-doped ZnO. [Reprinted from *Sensors and Actuators A: Physical*, 189, L. Chow, O. Lupan, G. Chai, H. Khallaf, L.K. Ono, B. Roldan Cuenya, I.M. Tiginyanu, V.V. Ursaki, V. Sontea, A. Schulte, *Synthesis and characterization of Cu-doped ZnO one-dimensional structures for miniaturized sensor applications with faster response*, 399–408, Copyright (2013), with permission from Elsevier]

No differences in morphology were observed at concentrations as low as 0.5% Cu in comparison with pure ZnO as reported previously [8,12]. Figure 3 shows the X-ray diffraction (XRD) patterns of the Cu-doped ZnO nanorods deposited at 95 °C. The intense diffraction peaks of the ZnO deposition appeared at 31.77°, 34.43°, 36.27°, 47.53°, 56.61°, and 62.83°, which correspond to the (100), (002), (101), (102), (110), and (103) planes, respectively [6]. The intense peaks in the XRD patterns of samples clearly show the formation of the hexagonal wurtzite structure of ZnO (space group: $P6_3mc(186)$ or C_{6v}^4 (Schoenflies notation); $a = 0.3249$ nm, $c = 0.5206$ nm) [6]. The prominent (002) plane is observed in all samples (0%–3% Cu in ZnO), which is the most dense plane in wurtzite ZnO [6,13].

In order to investigate the influence of copper doping on the Raman scattering in ZnO nanostructures, room temperature micro-Raman spectra of all samples were explored. In group theory $\Gamma_{opt} = A_1(z) + 2B_1 + E_1(x,y) + 2E_2$, where x , y , and z represent the polarization directions. A_1 and E_1 modes are polar and split into TO-transverse optical and LO-longitudinal optical components [6]. The E_2 modes are Raman-active only. The B_1 modes are infrared and Raman-inactive or silent modes. It is known that the $E_2(\text{low})$ mode in zinc oxide is associated with the vibration of the heavy Zn sublattice and the $E_2(\text{high})$ mode involves only the oxygen atoms. The $E_2(\text{high})$ mode is characteristic of the wurtzite phase material [6,9]. Figure 4 shows the micro-Raman spectrum of Cu-doped ZnO along with the spectrum of the undoped ZnO for comparison. They are clearly indicative of good wurtzite structure of pure and doped ZnO material. No Raman peaks of CuO or Cu₂O appeared in the spectrum of the Cu-doped ZnO nanostructures, indicating no secondary phase in copper-doped samples, which is consistent with the XRD results. From Figure 4 one observes the effects of Cu-doping on the $E_2(\text{high})$ mode of ZnO since its intensity decreases. The Raman spectrum indicates a shift in signal at ~ 437 cm⁻¹ for Cu-doped ZnO, which was observed in ZnO:Cu grown by other techniques [6,14–16]. The Raman line of the $E_2(\text{high})$ mode becomes broad and weaker, which means that the wurtzite crystalline structure of ZnO is weakened by high Cu doping [6,14] and due to formation of complex defects $[Cu_{Zn} - Zn_i]^x$ in Cu-ZnO. The frequency shift was explained by alloy potential fluctuation using a spatial correlation model by Samanta et al. [17].

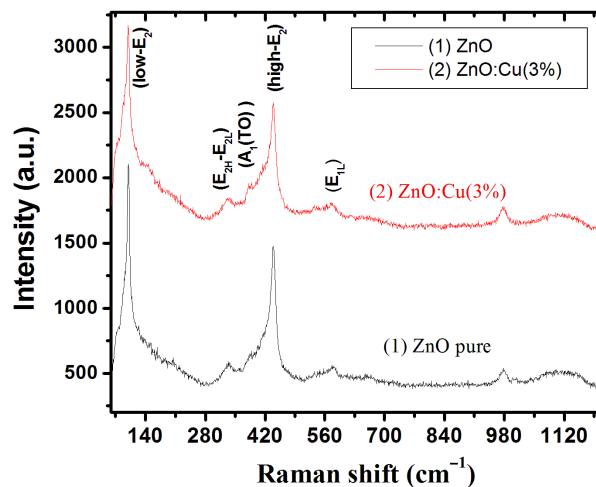


Figure 4. Micro-Raman spectra of pure ZnO and Cu-doped ZnO on Si substrates. [Reprinted from *Sensors and Actuators A: Physical*, 189, L. Chow, O. Lupan, G. Chai, H. Khallaf, L.K. Ono, B. Roldan Cuenya, I.M. Tiginyanu, V.V. Ursaki, V. Sontea, A. Schulte, *Synthesis and characterization of Cu-doped ZnO one-dimensional structures for miniaturized sensor applications with faster response*, 399–408, Copyright (2013), with permission from Elsevier]

The intense peak near 439 cm^{-1} due to the E_2 (high) mode (Figure 4, curve 1) displays a clear asymmetry toward low frequencies [6]. The asymmetric line shape was analyzed in detail by Cusco et al. [18]. It could be successfully explained in terms of resonant anharmonic interaction of the high- E_2 mode with a band of combined transverse and longitudinal acoustic modes, as the steep variation of the 2-phonon density of states around the high- E_2 frequency leads to a distorted phonon line shape. One can suggest that mixing 2 different cations through doping in aqueous solution could affect the local polarizability by charge distribution and result in at least 1 vibrational mode being strongly influenced [6,19,20].

3. Electrochemical deposition of ZnO nanowires

3.1. Electrochemical deposition of pure ZnO nanowires

Another cost-effective approach to synthesize zinc oxide nanostructures is electrochemical deposition (ECD). Well-aligned arrays of ZnO nanowires (ZnO NWs) were grown by the ECD method from a 0.2 mM ZnCl_2 (Merck, 99%) aqueous solution maintained at $85\text{ }^\circ\text{C}$ as reported before [21–24]. For the supporting electrolyte, 0.1 M potassium chloride (KCl) (Fluka, 98%) was employed to ensure a good electrical conductivity in the aqueous solution (Milli-Q quality water). The ZnO NWs were grown on conductive indium-doped tin oxide (ITO) film on a glass substrate with a sheet resistance of $15\ \Omega/\square$. Electrodeposition was carried out potentiostatically at -1.05 V using an Autolab PGSTAT30 potentiostat/galvanostat and with rotation of working electrode (WE) (with constant speed of $\omega = 300\text{ rpm}$) [24]. The potentiostat was monitored by the Autolab software. The pH of the solution was initially 5.5. The 3-electrode electrochemical cell was mounted in a thermoregulated bath and the temperature was fixed at $85\text{ }^\circ\text{C}$ with an uncertainty of $\pm 0.2\text{ }^\circ\text{C}$. The electrolyte was saturated with pure oxygen by bubbling for 45 min prior to the start of the electrolysis and continuously during the growth process. The growing process ended in 9000 s when the total passed/exchanged electrical charge reached 14.0 C/cm^2 [24].

In SEM images (Figure 5), the layer appears to be homogeneous and uniform. The nanowires are vertically oriented and well aligned. The average size is $\sim 160\text{--}220\text{ nm}$ in width and $\sim 4\text{--}5\ \mu\text{m}$ in length. Their density

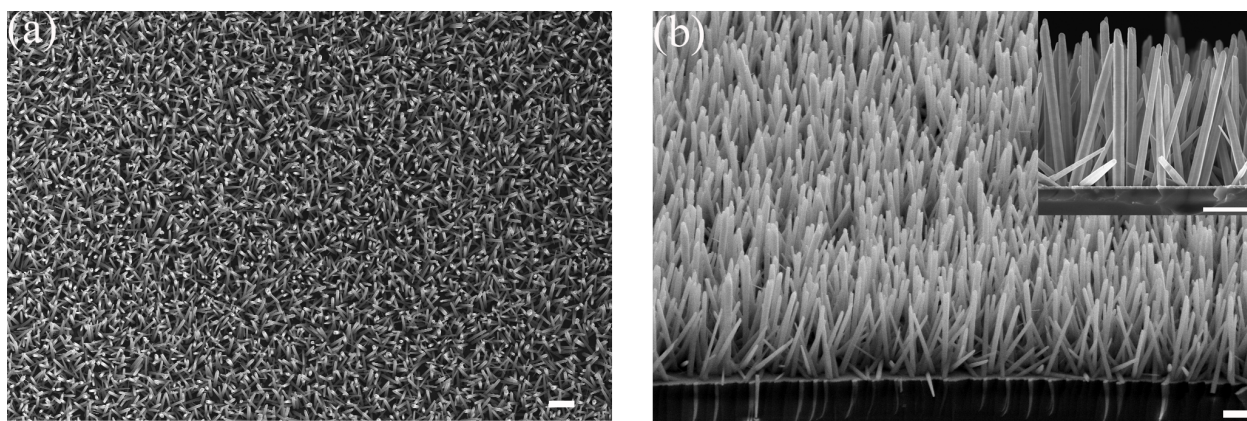


Figure 5. SEM images of ECD aligned ZnO nanowire arrays on ITO-glass: (a) plane view; (b) tilted view (65°), inset shows side-view of ZnO NWs forming arrays. Scale bar is $1\ \mu\text{m}$. [Reprinted from *Journal of Photochemistry and Photobiology A: Chemistry* 211, O. Lupan, V.M. Guérin, I.M. Tiginyanu, V.V. Ursaki, L. Chow, H. Heinrich, T. Pauporté, *Well-aligned arrays of vertically oriented ZnO nanowires electrodeposited on ITO-coated glass and their integration in dye sensitized solar cells*, 65–73, Copyright (2010), with permission from Elsevier]

is low at 4–5 NWs per μm^2 . There is excellent adherence and connection between the ZnO NWs and ITO substrate (Figure 5, inset) [24].

3.2. Electrochemical deposition of doped ZnO nanowires

The electrodeposition procedure was performed in a classical 3-electrode electrochemical cell using a solution containing 0.2 mmol L^{-1} ZnCl_2 , 0.1 mol L^{-1} KCl as a supporting electrolyte, and continuous bubbling of oxygen in a bath solution [21–28]. Two different concentrations of CuCl_2 (99.99% $\text{CuCl}_2 \cdot 2\text{H}_2\text{O}$, Aldrich) were investigated ($3 \mu\text{mol L}^{-1}$ and $6 \mu\text{mol L}^{-1}$) [27]. The substrates used were glass sheets coated with F-doped polycrystalline SnO_2 (FTO) (resistance of $10 \Omega/\square$). The FTO substrates were mounted as a WE for electrochemical deposition. Before deposition, the substrates were cleaned sequentially in acetone and then ethanol (95%) for 6 min each in an ultrasonic bath, followed by rinsing with abundant DI water ($18.2 \text{ M}\Omega \text{ cm}$) flow. Afterwards, these substrates were immersed in HNO_3 (45%) for 2 min in the ultrasonic bath and finally cleaned in DI water in the ultrasonic bath for 5 min and dried in air flux. The conducting cleaned FTO substrate was used as the WE. Contacts were performed with Cu wire and at the end by In-Ga eutectic to ensure good conductivity between the substrate that acted as the WE and the rotating support. Electrodeposition was carried out potentiostatically at -1.0 V versus the SCE reference electrode using an Autolab PGSTAT30 potentiostat/galvanostat and rotating WE (with constant speed of $\omega = 300 \text{ rpm}$) [27]. More details can be found in a previous report [27]. Afterwards it was subjected to thermal annealing in air at $250 \text{ }^\circ\text{C}$ for 10 h. The epitaxial ZnO NWs were grown on *p*-GaN (TDI Inc. Corporation) according to the procedure described elsewhere [26,27]. The deposition time was 5400 s. The heterojunction was annealed for 10 h at $250 \text{ }^\circ\text{C}$. In experiments performed by Lupan et al. [27], 3 sets of samples were prepared: #1 – pure ZnO NWs; #2 and #3 – ZnO NWs grown from a bath containing 3 and $6 \mu\text{mol L}^{-1}$ $\text{CuCl}_2 \cdot 2\text{H}_2\text{O}$ in electrolyte, respectively [27].

Figure 6a shows typical cyclic voltammograms of the real FTO–electrolyte interface recorded upon a first voltammetry scan started at the rest potential on the bare FTO electrode [27]. It was recorded in zinc chloride solution (0.2 mmol L^{-1}) under continuous oxygen bubbling. Oxygen was bubbled for 60 min before starting the experiment. When both zinc and oxygen are present in the electrolyte, one can observe a cathodic wave starting at -850 mV vs. SCE with a maximum current density of 0.86 mA/cm^2 at -1.3 V vs. SCE , which can be assigned to the electrochemical reduction of molecular oxygen. The small hysteresis is due to the covering of the FTO surface by ZnO upon the forward scan [27,28]. In the reverse scan, the current density decreased rapidly for pure ZnO (Figure 6a, curve 1). In the case of the solution containing Cu(II), the current on the negative-going scan was higher, showing an electrocatalytic effect of the deposited layer for molecular oxygen reduction. This was confirmed on the positive-going scan with the presence of a diffusion plateau extending over 360 mV (Figure 6a, curves 2 and 3). Afterwards, the reverse scan current decreased rapidly from -940 mV vs. SCE , with a monotonic decrement up to -350 mV vs. SCE , and then leveled off with a weak peak current of $30 \mu\text{A cm}^{-2}$ for pure ZnO (curve 1) and more evident anodic peaks of current for curves 2 and 3. The crossover between anodic and cathodic scans is evident and can be assigned to the deposition of metallic Zn under sufficiently negative polarization and its reoxidation at positive potentials. The anodic shift of the cathodic scan becomes prominent with increasing CuCl_2 concentration from 3 to $6 \mu\text{mol L}^{-1}$ in the bath. One can also observe 2 successive cathodic waves on the positive-going scan, which are the signature of the presence of copper [27].

From Figure 6a, a deposition potential of -1.0 V was chosen for the synthesis of the NWs due to the

window between -0.8 V and -1.2 V (vs. SCE) suitable for ZnO formation in the presence or absence of copper [27]. In Figure 6b, growth curves at constant applied potential of -1 V/SCE for samples #1–3 on FTO with a rotation speed of 300 rpm are shown. Line 1 corresponds to the deposition of pure ZnO. Lines 2 and 3 represent curves for baths with $3 \mu\text{mol L}^{-1}$ and $6 \mu\text{mol L}^{-1}$ CuCl_2 respectively at $T = 90^\circ\text{C}$.

Figure 7 shows the SEM images of pure and Cu-doped ZnO NWs grown on FTO substrates at 90°C . Figure 7a shows a top view of pure ZnO NWs grown on FTO substrate. Figure 7b is a cross-sectional view (90°) of pure ZnO NWs/FTO and Figure 7c depicts the SEM image of ZnO:Cu (1.2%) NWs on FTO substrate. No difference in SEM images was found between pure ZnO and ZnO:Cu (0.8%). No second phase could be observed even at the highest concentration. Analyses by energy dispersive X-ray spectroscopy were done to estimate the atomic Cu content in the films prepared in the presence of copper chloride [27].

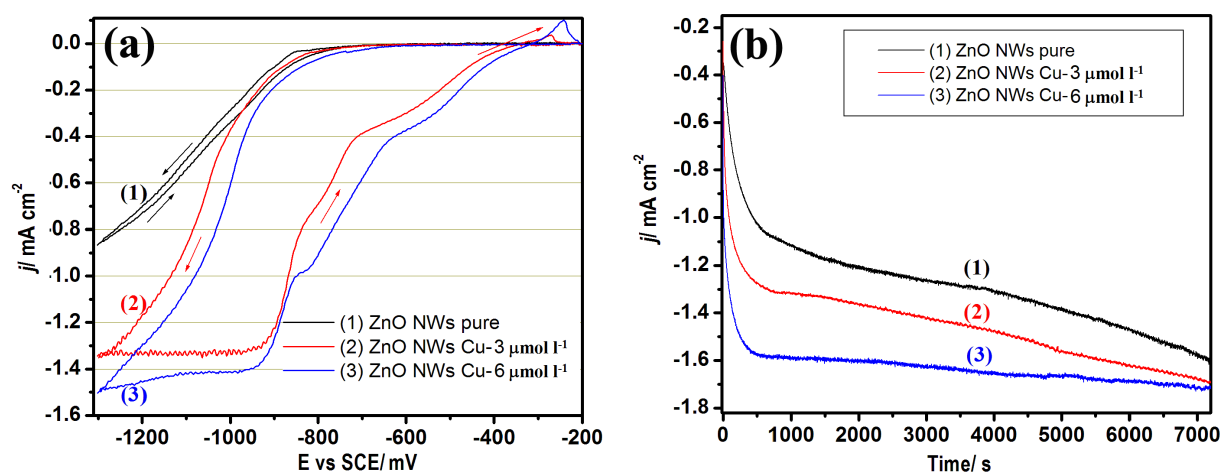


Figure 6. (a) Cyclic voltammograms of ZnO NWs on FTO substrates. First scan in the deposition bath containing 0.2 mmol L^{-1} ZnCl_2 in 0.1 mol L^{-1} KCl and various concentrations of copper ZnO. Scan rate: 10 mV s^{-1} . (b) Growth curves at constant applied potential of -1 V/SCE for samples #1–3 on FTO with a rotation speed of 300 rpm. Curve 1 corresponds to pure ZnO NWs. Curves 2 and 3 represent ZnO NWs for baths with $3 \mu\text{mol L}^{-1}$ and $6 \mu\text{mol L}^{-1}$ CuCl_2 , respectively. $T = 90^\circ\text{C}$. [Reprinted from *Electrochimica Acta*, 56, O. Lupan, T. Pauporté, B. Viana, P. Aschehoug, *Electrodeposition of Cu-doped ZnO nanowire arrays and heterojunction formation with p-GaN for color tunable light emitting diode applications*, 10543– 10549, Copyright (2011), with permission from Elsevier]

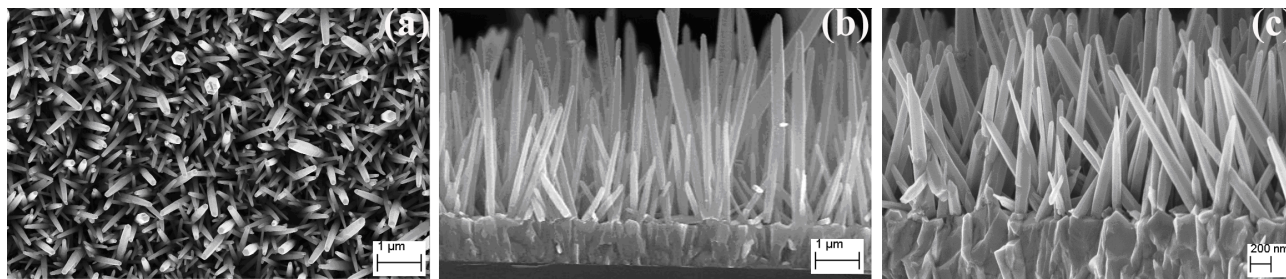


Figure 7. SEM micrographs of ZnO nanowires: (a) top view and (b) side view of pure ZnO NWs grown at 90°C , and (c) side view of ZnO:Cu (1.2%) nanowires electrodeposited on FTO substrate at 90°C . [Reprinted from *Electrochimica Acta*, 56, O. Lupan, T. Pauporté, B. Viana, P. Aschehoug, *Electrodeposition of Cu-doped ZnO nanowire arrays and heterojunction formation with p-GaN for color tunable light emitting diode applications*, 10543– 10549, Copyright (2011), with permission from Elsevier]

The molar ratio between copper and zinc in the ZnO NWs increased with the copper bath content and was significantly lower than that in the deposition bath. $[\text{Cu}]/[\text{Zn}+\text{Cu}]$ at.% content in zinc oxide nanowires was found to be about 0.8% and 1.2% for samples #2 and #3, respectively [27].

XRD studies of the crystal structure indicated only peaks of ZnO in pure and in Cu-doped ZnO NWs, along with the reflections from the FTO substrate (Figure 8) [27]. Figure 8a shows the XRD patterns recorded in the range of 10° – 90° with a scanning step of 0.02° of pure- and Cu-doped ZnO NWs. The pattern matches the lattice spacing of crystalline ZnO in the wurtzite structure (space group: $P6_3mc(186)$; $a = 0.3249$ nm, $c = 0.5206$ nm). The data are in agreement with the Joint Committee on Powder Diffraction Standards (JCPDS) card for ZnO (JCPDS 036-1451) [13]. XRD shows overexpression of the (002) plane, suggesting a preferential growth direction for most of the NWs. Since no copper-related peaks were observed after annealing in XRD patterns, the formation of Cu-based clusters on ZnO nanowires can be excluded within the detection limit [27]. This means that copper does not change the wurtzite structure of ZnO. However, a shift of about 0.031° or 0.061° to higher 2θ values of ZnO(002) peak can be clearly seen for ZnO:Cu ($3 \mu\text{mol L}^{-1}$) and ZnO:Cu ($6 \mu\text{mol L}^{-1}$), respectively, compared to pure ZnO (sample #1). A shift is also detected for ZnO(100). These shifts agree with previous reports [27,29–31].

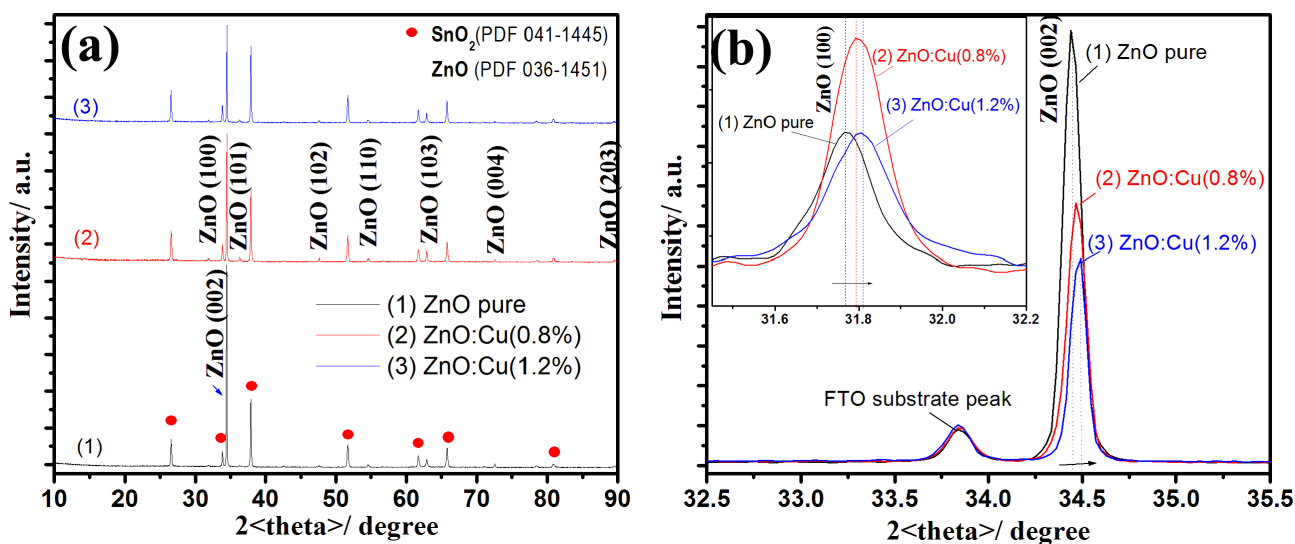


Figure 8. (a) XRD patterns of the pure and Cu-doped ZnO nanowires on FTO substrates. (b) Slow scans of the (100) and (002) peaks for the same samples (#1–3) are presented for viewing the lattice shrinking. [Reprinted from *Electrochimica Acta*, 56, O. Lupan, T. Pauporté, B. Viana, P. Aschehoug, *Electrodeposition of Cu-doped ZnO nanowire arrays and heterojunction formation with p-GaN for color tunable light emitting diode applications*, 10543–10549, Copyright (2011), with permission from Elsevier]

To study the effect of Cu-doping on the crystallinity of the ZnO nanowires, the intensities of the (100) and (002) diffraction peaks were monitored as shown in Figure 8b. The intensity of the diffraction peaks (100) increased for Cu-doping in sample #2 and remained the same for sample #3 compared to pure ZnO NWs (see Figure 8b). However, the full width at half maximum (FWHM) increased for Cu-doped samples (see Figure 8b), as presented in detail below [27].

As shown in Figure 8b, the ZnO XRD diffraction peaks are shifted by $\sim 0.06^\circ$ to higher 2θ angles for

Cu-doped ZnO NWs grown with $6 \mu\text{mol L}^{-1}$ CuCl_2 in solution compared to pure ZnO NWs. The change of FWHM from 0.149° (pure ZnO) to 0.175° ($6 \mu\text{mol L}^{-1}$ Cu-doped ZnO) of the (100) peak suggest the incorporation and disorder in lattice due to Cu. Such changes in crystallinity might be the result of changes in the atomic environment due to extrinsic doping on ZnO samples [23,27].

4. Device applications from ZnO nano- and microstructures

4.1. Nanofabrication of undoped ZnO nanosensors by in situ lift-out technique

In this section, the in situ lift-out technique used to fabricate nano- and microdevice structures is described. Si/SiO₂ wafers were used as intermediate substrates for ZnO tripod transferring and distribution in order to avoid charging problems in the FIB system. For the nanosensor preparation, a glass substrate was used and Al electrodes were deposited as a template with external electrodes/connections [8]. Usually a microscope and a micromanipulator for the ex situ lift-out technique are used to separate individual ZnO nanorods in order to be easily attached to the in situ FIB needle [8]. A magnification of $100\times$ was used to separate ZnO nanorods transferred to intermediate Si/SiO₂ substrate and distribute them on the surface for easy pick-up. A magnification of $6500\times$ was used to position a needle on the ion optic axis and to lift the single ZnO branched nanorod-tripod away from the Si/SiO₂ substrate [8].

A micromanipulator mounted beside the stage used in our work permits movements on the nanometer scale along the x , y , or z directions. A sample on the stage can be independently rotated perpendicular to the ion beam, which enables easy arrangement of single ZnO branched nanorod on the nanosensor template with Al contacts as external electrodes [8].

In the in situ process [8,32], it is found that attaching a single intermediate nanorod on the FIB needle (Figure 9a) allows for easy pick-up of the branched rod for further handling. This intermediary rod can greatly enhance the nanofabrication capability and reduce the number of steps in the procedure and the total time for nanodevice fabrication [8].

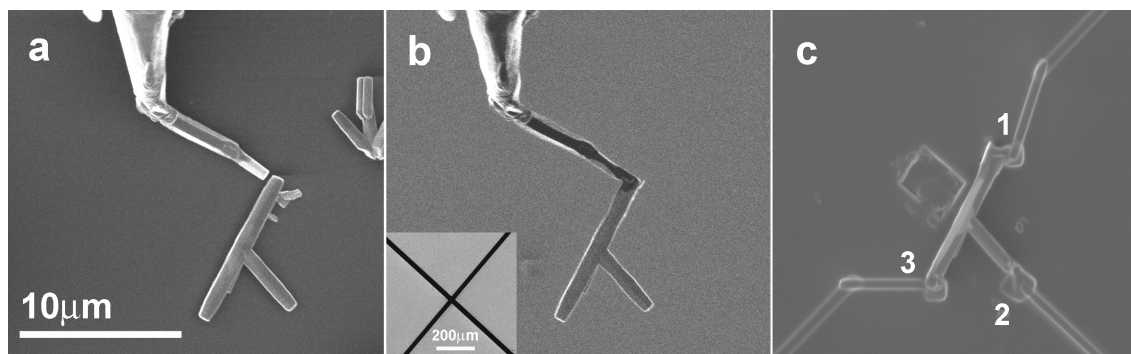


Figure 9. Scanning electron micrographs showing the steps of the in situ lift-out fabrication route in the FIB/SEM system: (a) branched ZnO nanorod transferred to Si/SiO₂ substrate and FIB needle positioned with intermediate connection using a single ZnO nanorod, (b) branched ZnO nanorod picked up by in situ lift-out needle to be used as tripod selected for nanofabrication, where inset shows the nanosensor substrate template (glass substrate with Al contacts as external electrodes); (c) branched nanorod cut from the needle, brushed to the sensor template support, and fixed to 3 electrodes/external connections to form the final nanosensor. [Reprinted from *Microelectronics Journal*, 38, O. Lupan, G. Chai, L. Chow, *Fabrication of ZnO nanorod-based hydrogen gas nanosensor*, 1211–1216, Copyright (2007), with permission from Elsevier]

The next step in this procedure was to scan the surface of the intermediate Si/SiO₂ substrate for placement of the ZnO nanorod-tripod. The needle was then lowered to the FIB focus with its tip positioned at the close end of the branched nanorod, as shown in Figure 9a [8]. Before attaching the selected branched nanorod it is recommended to push it in order to make sure that it is not attached firmly to the substrate and that the branches are strong enough to be transferable. The needle was then lowered until the tripod was attached to the end of the FIB needle, as shown in Figure 9b, using Pt deposition of 0.5 μm in thickness. Following this step (Figure 9b), the needle and specimen were moved away from the substrate [8].

Figure 9c shows the nanorod on the substrate using a micromanipulator on the nanodevice substrate/template (see inset in Figure 9b) with predeposited Al external electrodes. In this step, the needle was lowered and repeatedly swept across the substrate until the nanorod brushed against the support and became attracted to it. If the nanorod does not initially lie flat on the substrate, then it will be extremely difficult to realize good contacts with external electrodes. This situation will often happen in the case that an intermediate nanorod is not used or if the selected nanorod is not flat on the intermediate Si/SiO₂ substrate (Figure 9a) [8]. The last step consists of positioning of the tripod nanorod, then fixing it to one of the predeposited external electrodes. The nanorod is then cut and the needle raised away from the substrate. Figure 9c shows the single ZnO branched nanorod-based sensor fabricated by this nanotechnology [8]. The typical time taken to perform this in situ lift-out FIB nanofabrication is 30–45 min. The nanorod synthesis being done in 10 min contributed to overcoming some obstacles and the conception that nanorods/nanowires are not convenient [33] for sensor production. The technique as described in detail makes it easier to learn and apply nanofabrication steps using easily transferable nanorods (avoiding nanorods agglomerations) fabricated by our method, especially for new users/operators, and will permit the highest success rate. The authors' success rate using this route with the described steps was >90%. This minimizes the total time to machine time using FIB/SEM for the experimental nanodevice fabrication and can be extended for other specific devices [8].

Furthermore, this technology was extended for fabrication of new devices from a more complex nano- and microarchitecture [8,34,35]. Next, it was described how to fabricate a device from an individual ZnO tetrapod. To separate an individual ZnO tetrapod for further processing, an in situ FIB micromanipulator needle was used for the in situ lift-out purpose. Details on the in situ lift-out procedure were described in previous works [5,8,12,34,35]. Lupan et al. [35] found that it was much more difficult to fabricate individual tetrapod-based devices in comparison with the single nanorod/nanowire devices. The main difficulties to be overcome are: 1) an individual ZnO tetrapod has to be transferable from one substrate to another (Figure 10a); 2) the angles of tilt in the FIB chamber must be well aligned with both the initial substrate (Figure 10a) and the template substrate (Figure 10b); 3) the FIB needle with tetrapod (Figure 10b) must be positioned very accurately with nanometer precision in order to avoid breakage of the tetrapod junction. Three metal contacts were fabricated in order to connect external Au electrodes with the 3 legs of an individual ZnO tetrapod on glass substrate (Figure 10b). The fact that the tetrapod is a 3D object makes it more difficult in general [35].

First the intermediate nanorod was attached to the FIB micromanipulator tip as described in previous works [5,8,12,35]. Previous studies [5,8,12,34–36] found that attachment of a single intermediate rod on the top of the FIB micromanipulator tip will permit an easy pick-up of the selected tetrapod to be further handled. Next, the tip of the intermediate nanorod is brought into focus and lowered toward the ZnO tetrapod. The tip is positioned at one leg of the ZnO tetrapod and connected to one leg of the ZnO tetrapod as shown in Figure 10b. FIB-enhanced chemical vapor deposition is then used to deposit Pt thin film of 0.5 μm in thickness to join the tip to one leg of the ZnO tetrapod [35].

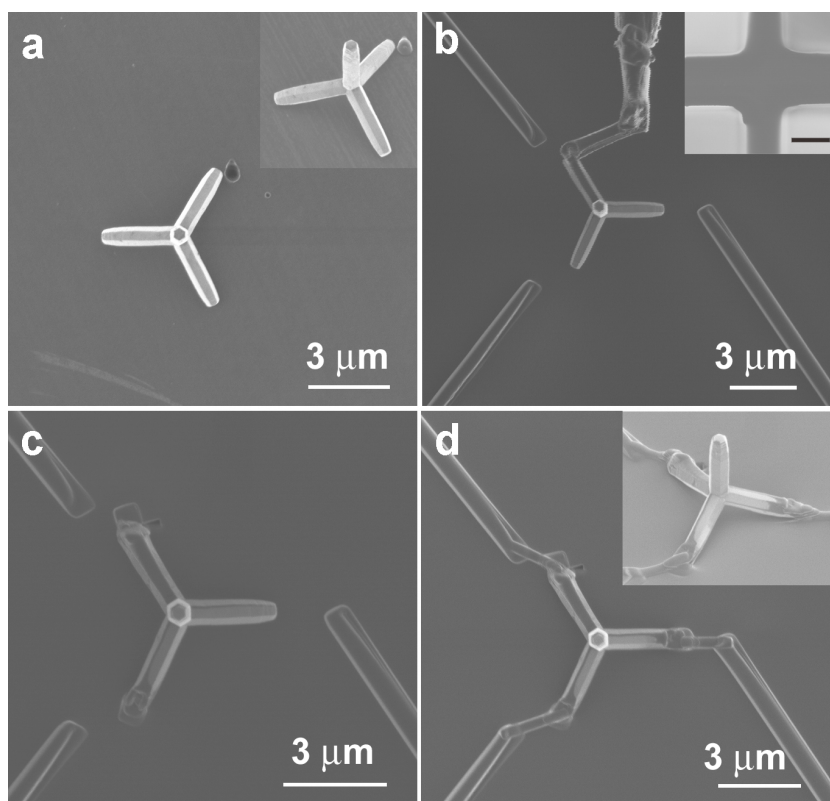


Figure 10. Secondary electron images showing the ZnO tetrapod and the steps of the in situ lift-out fabrication procedure in the FIB/SEM system. (a) A single ZnO tetrapod on Si substrate, viewed directly from above along the z -axis (inset shows side view of the ZnO tetrapod). (b) Tungsten needle with an intermediate rod attached to one of the legs of a ZnO tetrapod selected for sensor fabrication. It is placed next to external electrical connections. Inset shows the glass substrate with Cr/Au pads as contact electrodes ($10\ \mu\text{m}$ scale bar). (c) ZnO tetrapod is placed on the substrate and next to external gold electrodes. (d) ZnO tetrapod after connecting its 3 legs to the 3 external connections. Inset shows the side view of a single ZnO tetrapod sensor, $3\ \mu\text{m}$. [Reprinted from *Sensors and Actuators B: Chemical*, 145, O. Lupan, L. Chow, G. Chai, A single ZnO tetrapod-based sensor, 511-517, Copyright (2009), with permission from Elsevier]

In the next step, the tetrapod was transferred and then mounted with one leg to the sensor substrate by using FIB-enhanced chemical vapor deposition with Pt deposition (Figure 10c). The tetrapod was cut from an anchor point (end of intermediate point nanorod) and the needle rose away from the substrate (Figure 10c). Figure 10d shows the fabricated single tetrapod-based sensor with 3 legs connected to external electrodes. The fourth arm is pointing upward. The main advantage of this in situ lift-out procedure is a quick verification/testing of the concept of novel device designs in addition to being compatible with micro-/nanoelectronic device fabrication [35].

Figure 11 shows the gas response of the ZnO tetrapod-based multiterminal sensor to $100\ \text{ppm}\ \text{H}_2$ at room temperature. When exposed to $100\ \text{ppm}\ \text{H}_2$, a sharp increase and then slow decrease in the gas response was observed [35].

When a pulse of hydrogen was introduced, the response increased sharply again followed by a saturation region. All responses were studied for different leg pairs and we found that they were all similar to each other; therefore, only results from 1–2 will be presented here [35].

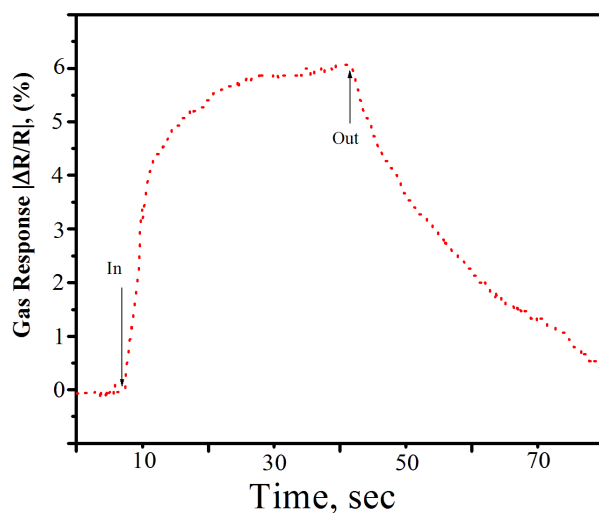


Figure 11. Responsivity of the ZnO tetrapod sensor to 100 ppm H₂ gas at the room temperature. [Reprinted from *Sensors and Actuators B: Chemical*, 145, O. Lupan, L. Chow, G. Chai, *A single ZnO tetrapod-based sensor*, 511-517, Copyright (2009), with permission from Elsevier]

Figure 12 shows the response test of a ZnO tetrapod-based sensor in various gas environments such as 100 ppm H₂, CO, *i*-butane, CH₄, CO₂, and SO₂ at room temperature. It is noted that the response to H₂ and CO gas is significantly higher than those to other gases. For a single ZnO tetrapod sensor, the response to 100 ppm H₂ is >6 times higher than the response to 100 ppm CH₄, CO₂, and SO₂ [35].

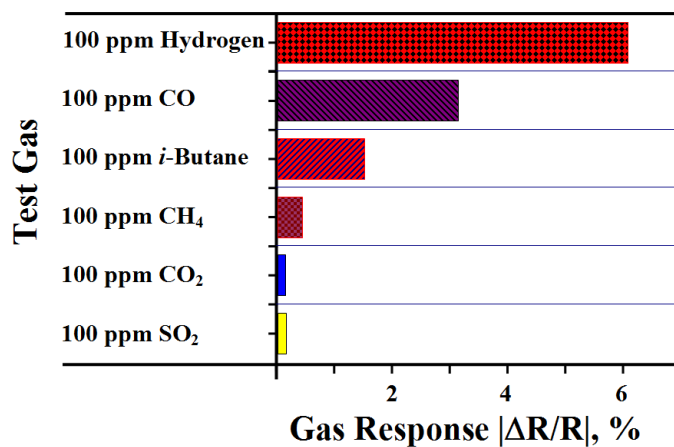


Figure 12. Gas response of ZnO tetrapod-based sensor to different gases at 100 ppm concentration. [Reprinted from *Sensors and Actuators B: Chemical*, 145, O. Lupan, L. Chow, G. Chai, *A single ZnO tetrapod-based sensor*, 511-517, Copyright (2009), with permission from Elsevier]

Several factors determine the gas sensing mechanism of ZnO micro- and nanowire/nanorods [37]. Initially, when metal oxide wire is placed in air atmosphere, the adsorbed oxygen (O_2^- and O^-) extracts electrons from the conduction band and an electron depletion region is formed, which leads to the increase of the resistance of individual nanowire. The exchange of electrons between the bulk of ZnO NW and the surface states takes place within a surface layer [37]. The thickness of this surface layer is of the order of the Debye length/radius (λ_D). This exchange will contribute to the decrease of the net carrier density in the nanowire conductance channel.

This will also lead to band bending near the surface for conduction and valence bands. The gas response of the resistive sensors in ambient medium is given by the following equation [37]:

$$S = (G_g - G_a)/G_g \times 100\% = 4/D(\lambda_{D(a)} - \lambda_{D(g)}) \times 100\% = 4/D((k\varepsilon_0 k_B T/e^2 N_0)^{1/2} - (k\varepsilon_0 k_B T/e^2 N_0)^{1/2}) \times 100\%,$$

or by following [38]:

$$S = 4/D(\lambda_{D(a)} - \lambda_{D(g)}) = 4/D(\varepsilon\varepsilon_0/\varepsilon n_0)^{1/2}(V_{S_a}^{1/2} - V_{S_g}^{1/2}),$$

where G_g and G_a are the conductance of ZnO nanowires in H_2 gas and in air ambient, respectively, and n_0 is the carrier concentration in air. V_{S_a} and V_{S_g} are the adsorption-induced band bending in air and in H_2 gas, respectively. According to the last equation, enhancement of H_2 gas sensitivity can be realized by controlling the geometric factor ($4/D$), electronic characteristics ($\varepsilon\varepsilon_0/en_0$), and adsorption-induced band bending ($V_{S_a}^{1/2} - V_{S_g}^{1/2}$) due to adsorption on the ZnO nanowire surface. This can be done by doping, which is our next case, or by using modulation of operation temperature, which is not desirable for H_2 sensors on single ZnO nanowire as discussed above. Another way is to make use of geometric parameters, which was realized in our experiments [37].

4.2. Nanofabrication of sensors from doped ZnO nano- and microstructures by in situ lift-out technique

The in situ lift-out procedure, described in previous works [6,8,12,37], was used to fabricate a double rod-based sensor. Details of the FIB fabrication process can be found in previous works [6,8,12,37].

Briefly, first 4 external contacts were made, as shown in Figure 13a [6]. Under the second set of contacts a hole was cut in order to allow the entire surface of the wire to be exposed. This is a demonstration of a concept that can be built with different structures for a variety of possible future applications. The tungsten needle with an intermediate microrod was then used to place selected rods at designated places, as shown in Figures 13b and 13c [6]. Figure 13d shows the fabricated double-rod-based sensor used for comparison under the same conditions with a single ZnO rod and a single Cu-ZnO rod [6].

The fabricated double-rod ZnO and Cu-ZnO-based sensor was put in a test chamber to detect H_2 and other gases, such as O_2 , CH_4 , CO, LPG, and ethanol. It was found that with H_2 gas introduction the resistance of the sensor changed [6]. After the exposure to hydrogen, the sensor was maintained for a recovering period in air. The room-temperature sensitivity of the single-rod ZnO and single-rod Cu-ZnO sensor to 200 ppm H_2 is shown in Figures 14a and 14b [6]. Response time constants for Cu-ZnO are faster, on the order of 30 ms, and 40 ms after the H_2 test gas is injected the signal reaches the equilibrium value. The relative resistance changes were about 44% [6]. The resistance was restored to 10% above the original value within 50–90 ms of introducing clean air. This suggests a reasonable recovery time. The sensor showed relatively fast response and baseline recovery for 200 ppm H_2 detection at room temperature. For comparison, pure ZnO rod-based sensor gas response is shown in the same figure. Chow et al. [6] found that sensitivity was about 10 times lower with a much slower time response.

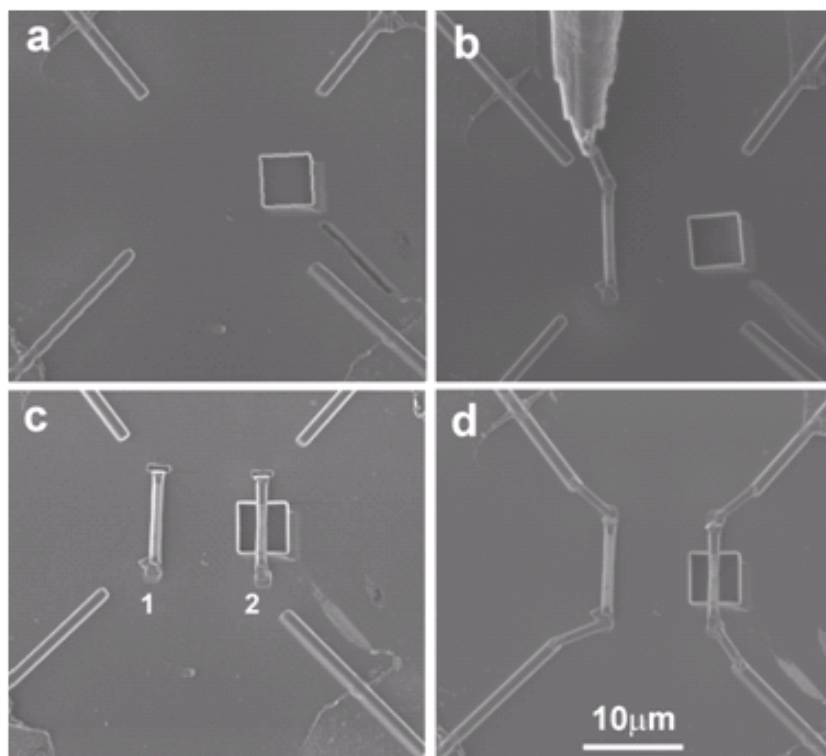


Figure 13. SEM images showing the steps of the in situ lift-out fabrication procedure in the FIB/SEM system. (a) Four external contacts prepared on the substrate, with a square hole cut on the glass substrate between 2 electrodes; (b) an intermediate ZnO rod and the main single ZnO rod selected for first sensor fabrication picked up by the FIB needle and positioned between the left 2 electrodes; (c) single ZnO rod #1 and single Cu-doped ZnO rod #2 selected for sensor fabrication placed between contact electrodes on the same substrate; (d) rods #1 (ZnO) and #2 (Cu-ZnO) both connected to electrode/external connections to form the final double rod sensor. [Reprinted from *Sensors and Actuators A: Physical*, 189, L. Chow, O. Lupan, G. Chai, H. Khallaf, L.K. Ono, B. Roldan Cuenya, I.M. Tiginyanu, V.V. Ursaki, V. Sontea, A. Schulte, *Synthesis and characterization of Cu-doped ZnO one-dimensional structures for miniaturized sensor applications with faster response*, 399–408, Copyright (2013), with permission from Elsevier]

For comparison, sensors made from rods with lower Cu-doping were also tested [6]. An improvement of sensor response was observed: about 25% and 35% for 0.5% Cu and 1% Cu doping, respectively. A significant improvement in comparison with pure ZnO-rod based sensors was obtained for rods doped in the range of 2%–3% Cu in ZnO and almost similar results were obtained, at about 40% and 44%, respectively. The resistance was restored to 10% above the original value within 25 s and 19 s after introducing clean air for 0.5% Cu and 1% Cu doping-ZnO sensors, respectively [6].

In order to test the selectivity to H_2 of our Cu-ZnO sensor, the response to C_2H_5OH , O_2 , CH_4 , and LPG was investigated and is summarized in Figure 14b [6]. One can see that the Cu-ZnO sensor's response to 200 ppm LPG and 200 ppm CH_4 is lower in comparison with its response to hydrogen. These data show the high selectivity of the fabricated sensor structure and the high prospect of Cu-doped ZnO as a material for miniaturized sensors operating at room temperature. Chow et al. [6] discussed the proposed sensing mechanism of a Cu-ZnO rod in comparison with pure ZnO. According to the results presented in Figure 14a, one can conclude that the Cu-ZnO sensor has a higher gas response and most importantly faster response and recovery times than the pure ZnO sensor. The factors influencing gas sensing properties of zinc oxide materials and their

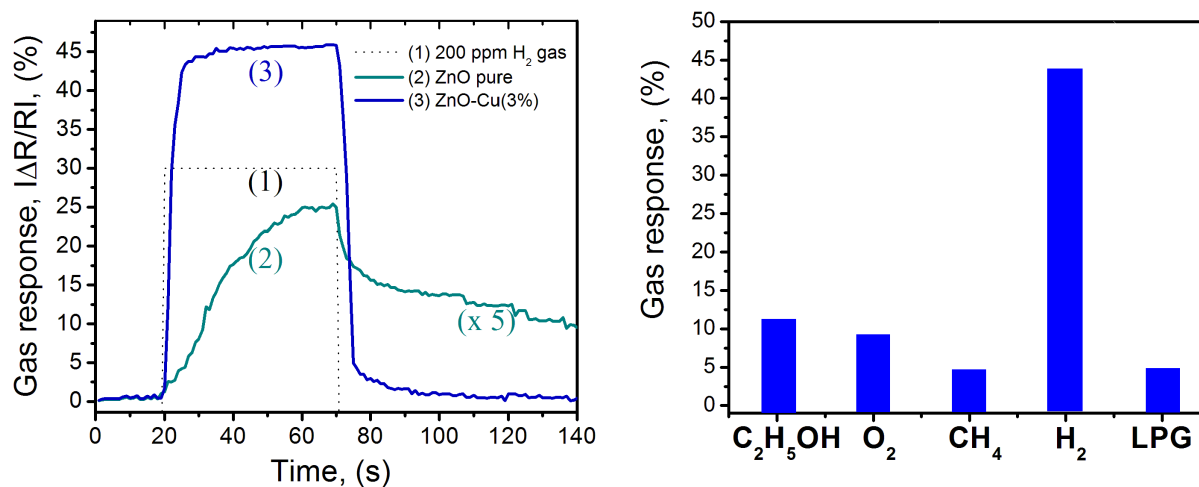


Figure 14. (a) The room temperature relative response (multiplied by 5) of the conductometric single ZnO rod (curve 2) and single Cu-doped ZnO (curve 3) rod-based sensor structure fabricated by in situ lift-out technique in the FIB system to 200 ppm H_2 gas pulse (curve 1). (b) Gas response of a Cu-ZnO rod based sensor to different ambient gases of 200 ppm concentration. [Reprinted from *Materials Science and Engineering: B*, 145, O. Lupan, L. Chow, G. Chai, B. Roldan Cuenya, A. Naitabdi, A. Schulte, H. Heinrich, *Nanofabrication and characterization of ZnO nanorod arrays and branched microrods by aqueous solution route and rapid thermal processing*, 57-66, Copyright (2007), with permission from Elsevier]

fundamental mechanisms are still under debate. However, one can conclude that the gas response is affected by depletion region sizes, concentrations of charge carriers, and defect states (e.g., oxygen vacancies V_O), which favors more oxygen to be adsorbed on the surface and respectively a higher gas response [6]. Another approach to improve the gas response is to use thinner and doped nanowires, which is described below.

4.3. Nanosensor applications from doped ZnO individual nanowire

Individually separated Cd-doped ZnO nanowires (NWs) were released from an array of as-grown NWs (see Lupan et al. [39]) by sonication in ethanol and subsequently transferred to a SiO_2 -coated Si substrate or by a direct contact of the sample with a clean Si wafer. Several devices were fabricated using Cd-ZnO NWs with lengths of between 2 and 3 μm and radii of between 40 nm and 100 nm, which showed reproducible electrical responses. The current-voltage (I-V) curves of the nanosensors measured at 300 K show a linear behavior [39]. The NW dark-resistance of $\sim 6 k\Omega$ in air at atmosphere pressure is assigned to oxygen molecules and water molecules adsorbed on the NW surface, which are expected to capture free electrons [37,39], as well as to the protonic conduction on the NW surface. The higher dark-resistance of $\sim 10 k\Omega$ in dry air is assigned to oxygen molecules adsorbed on the NW surface, which are expected to capture more free electrons. According to Lupan et al. [37,39], the gas response is defined as change of the resistance of the sensor in air versus the resistance in the test gas. Figure 15a shows the transient response of ZnO and Cd-doped ZnO-nanowire sensors (curves 1 and 2, respectively) of about 90 nm in diameter upon exposure to 100 ppm of H_2 gas at room temperature. As can be seen in Figure 15a (curve 2), both response (τ_r) and recovery times (τ_f) ($\tau = |t_{90\%} - t_{10\%}|$) were very fast for the Cd-ZnO NW, taking 14 s and 11 s for 90% full response and recovery, respectively. By comparing curve 2 for a Cd-ZnO NW with curve 1 for pure ZnO, a larger and quicker gas response was observed in the case of the doped NW sensor. The changes in the resistance of the sensor after exposure to hydrogen returned to

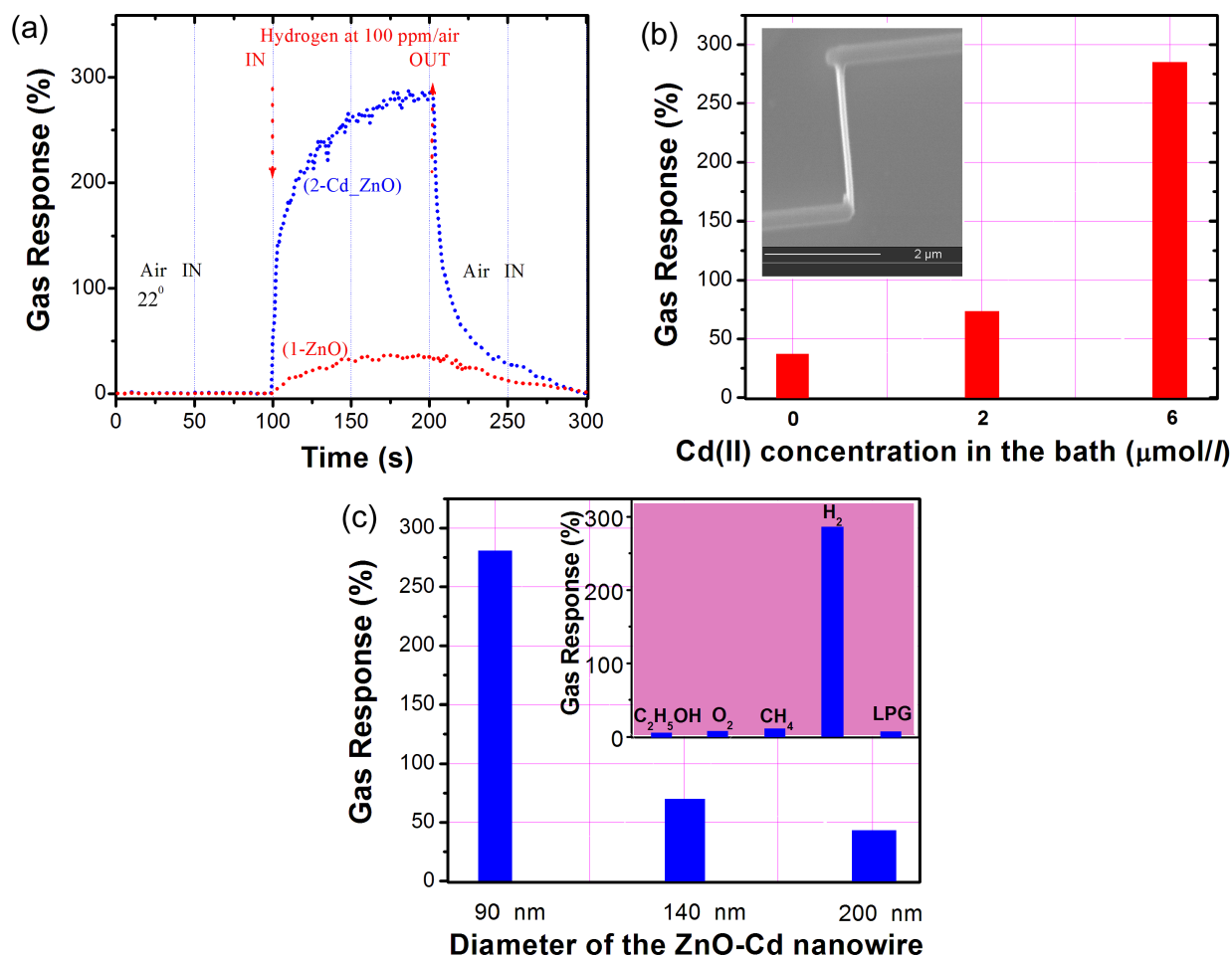


Figure 15. Room temperature gas responses of nanosensors based on a single pure ZnO NW and a ZnO-Cd (6 μM) NW of ~90 nm diameter versus (a) time and (b) the concentration of [Cd] (0-6 μM CdCl₂) in the electrolyte. For the Cd-doped ZnO NW, the gas response is also shown as a function of the NWs' diameter (90, 140, and 200 nm). In all cases, a 100 ppm H₂ gas pulse was used. The inset in (b) shows an SEM image of a single ZnO-Cd (6 μM) NW connected in a nanosensor configuration. The inset in (c) shows the gas response of the single Cd-ZnO NW-sensor to different gases (100 ppm H₂, 200 ppm others). All measurements were performed at room temperature. [Reprinted from *Sensors and Actuators B: Chemical*, 173, O. Lupan, L. Chow, Th. Pauporté, L.K. Ono, B. Roldan Cuenya, G. Chai, *Highly sensitive and selective hydrogen single-nanowire nanosensor*, 772-780, Copyright (2012), with permission from Elsevier]

within 10% of the initial value in about 11 s for the doped sample. This is explained by the presence of adsorbed gas molecules, which are desorbed from the surface of the doped ZnO NW faster than in the case of pure ZnO NW. Usually devices are operated at elevated temperatures or under UV light exposure in order to desorb the gas species from the surface of the sensor material [37,39]. In this case, the larger surface-to-volume ratio of the single-crystalline nanowires offers potential to improve the gas response and selectivity for hydrogen. The proposed gas sensing mechanism was discussed in detail by Lupan et al. [37] and presented above. It was used to develop nanosensors with better performances based on doped nanowires.

Figure 15b shows a comparison of the gas response of pure- and Cd-doped ZnO NW sensors (90 nm in diameter) [39]. It can be seen that by doping ZnO with cadmium the gas response to H₂ at room temperature

is improved. The inset in Figure 15b shows the single NW contacted by FIB. Figure 15c demonstrates the dependence of the gas response on the diameter of the Cd-ZnO NW-based sensors [39]. The highest gas response (about 274%) was obtained from a sensor based on a single Cd ($6 \mu\text{M}$)-doped ZnO NW with a 90 nm diameter [39]. For comparison, 140 nm and 200 nm ZnO NWs show lower responses to H_2 , namely less than 68% and 40%, respectively. Our results demonstrate the validity of thin doped ZnO NWs as H_2 sensors for low temperature operation conditions. Additionally, the power consumption of such nanosensors is $\sim 5 \text{ nW}$, which makes them very competitive for integration in wireless nanosensor networks. The existence of a depletion space charge region at the NW surface [37–40] can qualitatively explain the dependence of the gas response on the NW diameter (Figure 15c) [37].

The factors influencing gas-sensing properties of zinc oxide NWs and their fundamental mechanisms are still under debate. Lupan et al. [37,39] summarized the factors governing the sensing performance of single ZnO NW sensors. Such discussion can be extended to other metal oxide material nanowires as well. These are: 1) the diameter (D_{NW}) and aspect/ratio of the individual NWs [12,37], 2) gas-induced changes in the depletion region [41,42], 3) donor impurities in the NWs [43], 4) the surface potential [44], 5) adsorption/desorption enthalpy E_{des} [45], 6) surface functionalization or charged surface states N_s [46,47], 7) temperature of operation [48], and 8) ambient relative humidity RH [37,39,49,50]. Additionally, Lupan et al. [37,39] presented structural models of the conduction mechanism of single ZnO and Cd-ZnO NWs in air. Since V_s is the potential drop across the depletion layer, E_c is the lower edge of the conduction band and E_f is the Fermi level. Thus, for thicker NWs it can be concluded that the depletion layer does not influence the conduction channel as much as in the case of the thinner ZnO:Cd NWs [37,39]. In the latter example, the changes of the thickness of the depletion layer have a greater effect on the conduction channel, which leads to higher responses, in accordance with our experimental observations [37,39]. At the same time, it has to be considered that for a thin ZnO NW (50–100 nm), a Debye length of 20–50 nm is estimated from $d = \left(\frac{2\varepsilon_{ZnO}\varepsilon_0 V_s}{qn_e} \right)^{\frac{1}{2}}$ assuming n_e of about 10^{18} cm^{-3} and V_s ranging from 0.1 to 3 V [39,51]. Such a Debye length is comparable to the NW dimensions. For pure NWs with a diameter of 50–100 nm, the charge depletion region encompasses the entire NW, and flat-band conditions take place. For a high-purity stoichiometric ZnO NW, $\lambda_{D(a)}$ can be very large due to the decrease of the charge-carrier concentration. In this case, the position of the Fermi level shifts away from the band gap throughout the entire NW and the equilibrium between free electrons and ionized vacancies is achieved, and electrons move without the interference of the electrostatic barrier [39]. If a surface state is present at an energy level below E_f under the flat band condition, which applies to the NW in the radial direction, the electrons will be transferred from the E_c to these surface states and transfer will occur until E_f is constant throughout the surface and the interior of the NW (equilibrium state). Electrons will be distributed homogeneously in the volume of the NW and current flow cannot be varied significantly by adsorbed H_2 molecules on the surface (especially at very low concentrations of ppm or ppb). On the other hand, for metals or degenerate semiconductors, $\lambda_{D(a)}$ is comparable to the dimension of the atom, which makes it possible to use only ultrathin layers as sensing material. Such ultrathin structures could however generate problems because of the stability of their connections.

In this situation, controlled doping (the density of the conduction electrons $n \sim N_d$) or functionalization of the surface is a good approach to tune λ_D (or the depletion region) and get enhanced gas response from ZnO NWs. That is why it is important to dope ZnO NWs and to control the position of the Fermi level inside the band gap [37,39]. Thus, it is possible to control sensitivity, selectivity, and response time of thinner doped NWs.

5. Conclusion

In this work we present an overview of nano-ZnO synthesis techniques at relatively low temperatures (<100 °C) and using cost-effective approaches. In addition, we summarize their micro- and nanodevice applications, especially for sensing different chemical species. It can be clearly seen that doped ZnO nano- and microstructures offer a possibility to improve sensorial performances for hydrogen gas. The sensing mechanism was discussed and summarized for pure and doped nanomaterials. Considering that hydrogen is a fuel of the future, this work provides an extremely important review for directing synthesis and multifunctional application of nano-ZnO for H₂ nanosensors.

Acknowledgment

This work was financially supported by the STCU and ASM through Grant 09 STCU.A/5833.

References

- [1] Özgür, Ü.; Alivov, Y. I.; Liu, C.; Teke, A.; Reshchikov, M. A.; Doğan, S.; Avrutin, V.; Cho, S. J.; Morkoç, H. *J. Appl. Phys.* **2005**, *98*, 041301.
- [2] Morkoc, H.; Özgür, Ü. *Zinc Oxide: Fundamentals, Materials and Device Technology*; Wiley: Hoboken, NJ, USA, 2009.
- [3] Tiginyanu, I. M.; Lupan, O.; Ursaki, V. V.; Chow, L.; Enachi, M. In *Comprehensive Semiconductor Science and Technology*, Volume 3; Pallab Bhattacharya, P.; Fornari, R.; Kamimura, H, Eds. Elsevier: Amsterdam, the Netherlands, 2011, pp. 396–479.
- [4] Lupan, O.; Chow, L.; Chai, G.; Roldan Cuenya, B.; Naitabdi, A.; Schulte A.; Heinrich, H. *Mater. Sci. Eng. B* **2007**, *145*, 57–66.
- [5] Chai, G.; Lupan, O.; Chow, L.; Heinrich, H. *Sens. Actuators A* **2009**, *150*, 184–187.
- [6] Chow, L.; Lupan, O.; Chai, G.; Khallaf, H.; Ono, L. K.; Roldan Cuenya, B.; Tiginyanu, I. M.; Ursaki, V. V.; Sontea, V.; Schulte, A. *Sens. Actuators A* **2013**, *189*, 399–408.
- [7] Lupan, O.; Pauporte, T.; Viana, B. *J. Phys. Chem. C* **2010**, *114*, 14781–14785.
- [8] Lupan, O.; Chai, G.; Chow, L. *Microelectronics J.* **2007**, *38*, 1211–1216.
- [9] Lupan, O.; Chow, L.; Ono, L. K.; Roldan Cuenya, B.; Chai, G.; Khallaf, H.; Park, S.; Schulte, A. *J. Phys. Chem. C.* **2010**, *114*, 12401–12408.
- [10] Lupan, O.; Pauporte, T.; Chow, L.; Chai, G.; Viana, B. Ursaki, V. V.; Monaco, E.; Tiginyanu, I. M. *Appl. Surf. Sci.* **2012**, *259*, 399–405.
- [11] Shishiyanu, S. T.; Lupan, O. I.; Shishiyanu, T. S.; Sontea, V. P.; Railean, S. K. *Electrochim. Acta* **2004**, *49*, 4433–4438.
- [12] Lupan, O.; Chai, G.; Chow, L. *Microelectron. Eng.* **2008**, *85*, 2220–2226.
- [13] American Society for Testing and Material. *Powder Diffraction Files; Joint Committee on Powder Diffraction Standards*; Swarthmore, PA, USA: American Society for Testing and Material, 2009.
- [14] Sharma, P. K.; Dutta, R. K.; Pandey, A. C. *J. Magnetism Magnetic Mater.* **2009**, *321*, 4001–4005.
- [15] Phan, T. L.; Vincent, R.; Cherns, D.; Nghia, N. X.; Ursaki, V. V. *Nanotechnology* **2008**, *19*, 475702.
- [16] Wang, Z.; Zhang, H.; Zhang, L.; Yang, J.; Yan, S.; Wang, C. *Nanotechnology* **2003**, *14*, 11–15.
- [17] Samanta, K.; Bhattacharya, P.; Katiyar, R. S.; Iwamoto, W.; Pagliuso, P. G.; Rettori, C. *Phys. Rev. B* **2006**, *73*, 245213.

- [18] Cuscó, R.; Alarcón-Lladó, E.; Ibáñez, J.; Artús, L.; Jiménez, J.; Wang, B.; Callahan, M. *J. Phys. Rev. B* **2007**, *75*, 165202.
- [19] Wang, X. F.; Xu, J. B.; Yu, X. J.; Xue, K.; Zhao, X. *Appl. Phys. Lett.* **2007**, *91*, 031908.
- [20] Windisch, C. F.; Exarhos, G. J.; Owings, R. R. *J. Appl. Phys.* **2004**, *95*, 5435.
- [21] Pauporté, T.; Bataille, G.; Joulaud, L.; Vermersch, F. J. *J. Phys. Chem. C* **2010**, *114*, 194–202.
- [22] Pauporté, T.; Jouanno, E.; Pellé, F.; Viana, B.; Ashehoung, P. *J. Phys. Chem. C* **2009**, *113*, 10422–10431.
- [23] Lupan, O.; Pauporté, T.; Chow, L.; Viana, B.; Pellé, F.; Ono, L. K.; Roldan Cuenya, B.; Heinrich, H. *Appl. Surf. Sci.* **2010**, *256*, 1895–1907.
- [24] Lupan, O.; Guérin, V. M.; Tiginyanu, I. M.; Ursaki, V. V.; Chow, L.; Heinrich, H.; Pauporté, T. *J. Photoch. Photobio. A* **2010**, *211*, 65–73.
- [25] Goux, A.; Pauporté, T.; Lincot, D. *Electrochim. Acta* **2006**, *51*, 3168–3172.
- [26] Lupan, O.; Pauporté, T.; Viana, B.; Tiginyanu, I. M.; Ursaki, V. V.; Cortés, R. *ACS Appl. Mater. Interfaces* **2010**, *2*, 2083–2090.
- [27] Lupan, O.; Pauporté, T.; Viana, B.; Ashehoung, P. *Electrochim. Acta* **2011**, *56*, 10543–10549.
- [28] Pauporté, T.; Lincot, D. *Electrochim. Acta* **2000**, *45*, 3345–3353.
- [29] Heng, T. S.; Lau, S. P.; Yu, S. F.; Yang, H. Y.; Wang, L.; Tanemura, M.; Chen, J. S. *Appl. Phys. Lett.* **2007**, *90*, 032509.
- [30] Chakraborti, D.; Narayan, J.; Prater, J. T. *Appl. Phys. Lett.* **2007**, *90*, 062504.
- [31] Zhang, Z.; Yi, J. B.; Ding, J.; Wong, L. M.; Seng, H. L.; Wang, S. J.; Tao, J. G.; Li, G. P.; Xing, G. Z.; Sum, T. C. et al. *J. Phys. Chem. C* **2008**, *112*, 9579–9585.
- [32] Chai, G.; Chow, L.; Zhou, D.; Byahut, S. R. *Carbon* **2005**, *43*, 2083–2087.
- [33] Wang, C.; Chu, X.; Wu, M. *Sens. Actuators B* **2006**, *113*, 320–323.
- [34] Lupan, O.; Pauporté, T.; Viana, B. *Adv. Mater.* **2010**, *22*, 3298–3302.
- [35] Lupan, O.; Chai, G.; Chow, L. *Sens. Actuators B* **2009**, *141*, 511–517.
- [36] Lupan, O.; Chow, L.; Chai, G.; Chernyak, L.; Lopatiuk, O.; Heinrich, H. *Phys. Status Solidi A* **2008**, *205*, 2673–2678.
- [37] Lupan, O.; Ursaki, V. V.; Chai, G.; Chow, L.; Emelchenko, G. A.; Tiginyanu, I. M.; Gruzintsev, A. N.; Redkin, A. N. *Sens. Actuators B* **2010**, *144*, 56–66.
- [38] Chen, P. C.; Shen, G.; Zhou, C. *IEEE T. Nanotechnol.* **2008**, *7*, 668–682.
- [39] Lupan, O.; Chow, L.; Pauporté, T.; Ono, L. K.; Roldan Cuenya, B.; Chai, G. Y. *Sens. Actuators B* **2012**, *173*, 772–780.
- [40] Goldberger, J.; Sirbuly, D. J.; Law, M.; Yang, P. *J. Phys. Chem. B* **2005**, *109*, 9–14.
- [41] Roldan Cuenya, B.; Kolmakov, A. In *Functional Nanostructures: Processing, Characterization, and Applications*; Seal, S., Ed. Springer: New York, NY, USA, 2008, pp. 305–344.
- [42] Fan, Z.; Wang, D.; Chang, P. C.; Tseng, W. Y.; Lu, J. G. *Appl. Phys. Lett.* **2004**, *85*, 5923.
- [43] Zhao, M.; Wang, X.; Ning, L.; Jia, J.; Li, X.; Cao, L. *Sens. Actuators B* **2011**, *156*, 588–592.
- [44] Fan, Z.; Lu, J. G. *Appl. Phys. Lett.* **2005**, *86*, 032111.
- [45] Zhang, Y.; Kolmakov, A.; Lilach, Y.; Moskovits, M. *J. Phys. Chem. B* **2005**, *109*, 1923–1929.
- [46] Zhou, J.; Gu, Y.; Hu, Y.; Mai, W.; Yeh, P. H.; Bao, G.; Sood, A. K.; Polla, D. L.; Wang, Z. L. *Appl. Phys. Lett.* **2009**, *94*, 191103.
- [47] Kuang, Q.; Lao, C. S.; Li, Z.; Liu, Y. Z.; Xie, Z. X.; Zheng, L. S.; Wang, Z. L. *J. Phys. Chem. C* **2008**, *112*, 11539–11544.

- [48] Wei, T. Y.; Yeh, P. H.; Lu, S. Y.; Wang, Z. L. *J. Am. Chem. Soc.* **2009**, *131*, 17690–17695.
- [49] Chai, G. Y.; Chow, L.; Lupan, O.; Rusu, E.; Stratan, G. I.; Heinrich, H.; Ursaki, V. V.; Tiginyanu, I. M. *Solid State Sci.* **2011**, *13*, 1205–1210.
- [50] Chai, G. Y.; Lupan, O.; Rusu, E. V.; Stratan, G. I.; Ursaki, V. V.; Şontea, V.; Khallaf, H.; Chow, L. *Sens. Actuators A.* **2012**, *176*, 64–71.
- [51] Goldberger, J.; Sirbuly, D. J.; Law, M.; Yang, P. *J. Phys. Chem. B* **2005**, *109*, 9–14.